Zernike coefficients of digital holographic optical elements

Jung-Young Son*[a], Tetiana Venkel[b], Jung Kim[a], J. M. Rodriguez-Ramos[c] and J. G. Marichal-Hernandez[c]
[a]Public Safety Research Center, Konyang University, Nonsan, 32992, Korea; [b]Linguistics for Sciences Department 26, Chernivtsi, 58012, Ukraine; [c]Industrial Engineering Department, Universidad de La Laguna, La Laguna, 38200, Spain
* jyson@konyang.ac.kr

ABSTRACT

The optical characteristics of digitally recorded holographic optical elements by the wavefront recording method are measured with a Shack-Hartmann wavefront sensor and their performances as an optical element are compared with those of a spherical mirror and an analog holographic optical element with use of the reconstructed wavefront by Zernike polynomial. The comparison shows that the digitally recorded holographic optical elements can work as a spherical mirror/lens, but it introduces wavefront aberration much more than the mirror and the analog holographic optical element.

Keywords: Digitally recorded holographic optical element, optical characteristics, Shack-Hartmann wavefront sensor, the reconstructed wavefront by Zernike polynomial, wavefront aberration

1. INTRODUCTION

The 1st digital hologram can be considered as the Zebra hologram which was known as a stereo hologram [1]. But there were multiple and composite holograms: The composite hologram was a collection of small size holograms. Each of the holograms works independently but the whole reconstructed images work cooperatively. The multiple hologram is the stereo hologram; it is recorded by dividing a photoplate into a number of equal dimension strips corresponding to that of the different view images to be recorded and then each view image is recorded its corresponding position strip. So, it consists of many strip-shape holograms. The Zebra hologram is a two dimensional version of the multiple hologram. Hence, it consists of a two-dimensional array of hologram spots names as hogels. Each hogel is the hologram of an image, which is made to have a dot shape with the diameter of near 1 mm. The image represented by a hogel is an image in a two-dimensional multiview image set for a light field imaging. The digital holographic optical element (DHOE) is made the same way as the Zebra Hologram. In this case, each hogel is not an image but a segmented piece of a wavefront pattern of an optical element. The HOE is a hologram which is made to work as an optical element. The most frequently used optical elements for the imaging in a typical optical laboratory are lenses and spherical mirror. However, these elements become heavier and bulky as their sizes increase. Holographic optical elements have been used to replace them and other optical element such as filters and diffusers because they can be made to have various optical parameters such as focal length, shape and size, on a plane photoplate/film [2]. The digitally recorded HOEs, i.e., DHOEs are more convenient than their analog version because they do not require any real optical elements to records the HOEs but needs only the elements' wavefront patterns. Since these patterns can be calculated by a computer, they can be made to have any optical parameter. This is the main reason of recording the DHOEs instead of the analog HOEs [3]. The typical wavefront pattern of a lens or a spherical mirror does not different from the fringe pattern of the hologram of a point or a Fresnel zone pattern. It will be easily calculated with a computer to have any needed parameters, focal length and focal spot position [4]. However, the DHOEs have several problems to solve: The 1st is how to reduce the recording time of each HOE. Since each HOE is consisted of an array of hologram spots representing the wavefront pattern, the recording time of are tremendous. The 2nd, since these spots work as the resolution elements for the reconstructed wavefront pattern, each spot size should be reduced as small as possible to make it invisible, i.e., unnoticed to the users. This size reduction will bring the problem of recording a greater number of spots in the array to make a HOE with a required dimension. It is obvious that the recording time will be increases. The 3rd, the recording time increase will affect the uniformity of the recording due to any internally and externally introduced instabilities to the recording set-up. Hence, there may be under exposed hologram spots, different hologram spot sizes and positions, overlapped and missed spots

Sixteenth International Conference on Correlation Optics, edited by Oleg V. Angelsky, Claudia Yu. Zenkova, Proc. of SPIE Vol. 12938, 1293821 · © 2024 SPIE · 0277-786X · doi: 10.1117/12.3014855

and so on. So these uniformity deteriorating factors can induce its reconstructed wavefront pattern to be distorted and partly blurred. These distortions and blurring in the reconstructed wavefront pattern will induce the wavefront aberration to the light beams which are passed through or reflected from the HOE. It is expected that the wavefront aberration will be increased as the HOE size increases. For this reason, the optical performances of the digitally recorded HOEs are measured with a wavefront sensor such as Shack-Hartmann wavefront sensor [5], the wavefront deviations achieved with the sensor are interpreted with the reconstructed wavefront of the HOEs with use of Zernike polynomial [6]. Furthermore, the performances are compared with those of a spherical mirror and an analog HOE for a head up display (HUD) [7,8] to show visually those of the DHOEs. Zernike polynomial is mathematically expressing the exit pupil wavefront deviation from that of the reference aperture sphere. Each component of the polynomial represents a specific aberration in an optical element.

In this paper, the optical performances of digitally recorded HOEs are compared with those of a spherical mirror and an analog HOE are compared with use of a phase map derived from the wavefront deviation measured with a Shack-Hartmann wavefront sensor and 2) the reconstructed wavefront which are derived by Zernike polynomial.

2. PREPARATIONS OF DHOES AND WAVEFRONT SENSOR

Two DHOE samples are prepared by the optical set-up similar to that for Zebra hologram recording [3]. For DHOE, a segmented piece of the wavefront pattern as shown in Fig. 1 is recorded as a hogel. The pattern is the fringe pattern of the hologram of a point object, calculated by a computer. This pattern also represents either a spherical mirror or a lens. It is segmented into pieces of having an equal dimension and each piece is displayed on a SLM. A collimated laser beam as an object beam illuminates the SLM. The reflected beam from or transmitted beam through the SLM will be focused as a small size collimated beam by a telecentric lens and then it will pass through a photoplate. A hogel will be recorded on the photoplate at the place where the collimated beam is passed when a collimated beam as a reference beam is incident to the place with a designed incident angle. To record another hogel at its right, the segment of the wavefront pattern at the right side of the segment corresponding to the hogel is loaded to the SLM by translating the photoplated to the left side with the distance corresponding to the horizontal dimension of the hogel [9]. The process will be repeated until complete all the segments of the wavefront pattern to record a DHOE. When a reconstruction beam illuminates the DHOE with the same beam incidence angle as the reference beam, the reflected beam from the DHOE will be focused to a light spot. Since the active surface shape of the SLM has a rectangle, the beam on the photoplate will have the same shape as the SLM's active surface. Hence each hogel will reconstruct the rectangle shape beam segment. Hence, the reconstructed image on the DHOE surface will be the same as the wavefront pattern to work as the spherical mirror or the lens. Each DHOE is recorded on a 50 mm x 50 mm silver halide photoplate with use of a green laser with 532 nm wavelength. Since the spot size of a hogel is 0.98 mm x 0.52 mm, the total number of hogels in the photoplate is 51 x 96.

Fig. 2 shows the two DHOEs which were made with the reference beam incidence angle of 45˚ and the designed focal length of 330 mm, and a spherical mirror and a analog HOE. The arrows in the DHOEs indicate the defected hogels. They are under-exposed, different shape and missed. It is also noticed that the hogels are not uniformly arranged. The border lines are zig-zagging. Furthermore, the DHOE reveals astigmatism. The least circle of confusion appears at 310 mm. This focal length is shorter than the designed. The spherical mirror has the diameter of 150 mm and the focal length of 220 mm. The analog HOE has the focal length of 500 mm and its dimension is 170 mm x 220 mm. Hence to illuminate these samples, the collimated beam diameter is made to have 50 mm. This beam will cover the entire DHOE surface but for the spherical mirror and the analog HOE, it illuminates normally to their central part.

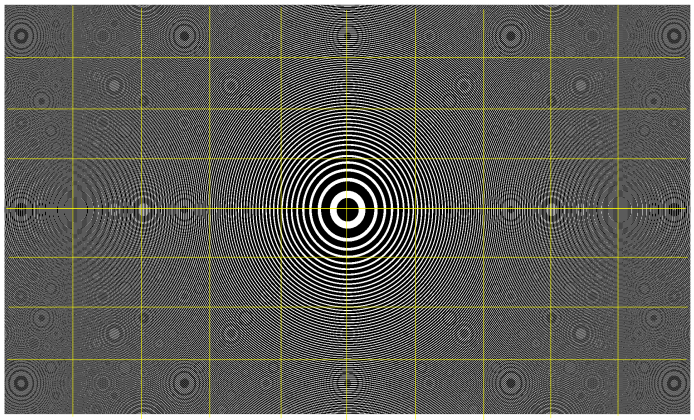

Figure 1. Wavefront pattern of a spherical mirror/lens: The pattern is segmented into 10 x 8 pieces.

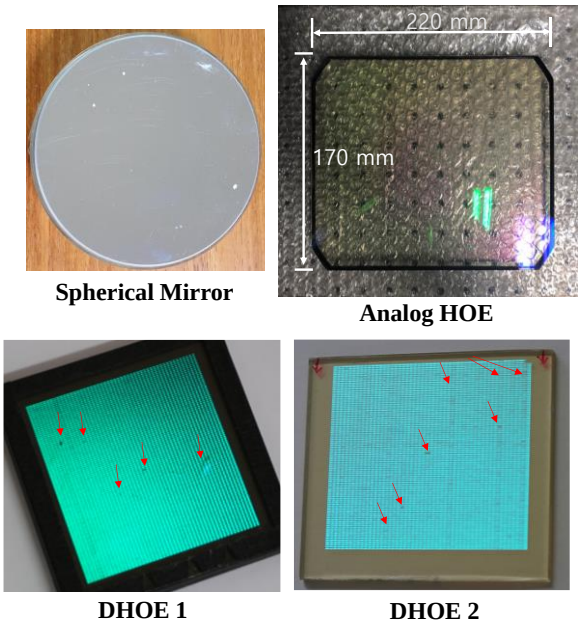

Figure 2. Samples for this paper: A spherical mirror, an analog HOE and two DHOEs. Each DHOE consisted of 51 x 96 hogels. The arrows indicate defects in the hogel array.

The Shack-Hartmann wavefront sensor consisted of a microlens array and CMOS detector. The array consists of 77 x 51 microlenses and the array of 6000 x 4000 pixels. Each microlens has the dimension of 300 μm x300 μm and focal lengths of 2 mm. Since each pixel has the dimension of 3.89 μm x 3.89 μm, each microlens corresponds to 77 x 77 pixels. The beam coming normally to the microlens array will be focused at the center of the 77 x 77 pixels array. However, the beam with certain beam incidence angle to a microlens will be focused at other place in the pixel array. Hence, the maximum beam incidence angle of the beam, that can be focused within the 77 x 77 pixels array is defined as 4.29˚ by the focal length and the microlens diameter. This is the maximum wavefront deviation that can be detected without uncertainty. Those beams exceeding the angle will be focused at its neighboring pixel arrays. The wavefront aberration is caused by the materials in the path of a beam. The beam propagation direction will be changed by the materials and its phase can be delayed since the light speed is inversely proportional to the refractive indices of the material. So, the beam

direction and speed changes induce the beam's wavefront to be aberrated. Hence any departure of the material quality from that of the reference material will induce the wavefront aberration. This is why a microlens array is needed: Smaller the microlens size, more detailed local wavefront aberration changes will be detected. er, In the sensor, the aberration is represented by the focused point deviation from the center of the pixel array. This is the principle of the sensor. It is shown in Fig. 3. The material in the right side has different refractive index from that of left part. So, the beam incident direction to the microlens is changed. The focused position of the beam will be determined by the centroid calculation [10] in the coordinate quadrant. This quadrant position represents the wavefront aberration and the Zernike polynomial is calculated from the ratio of the position to the focal length of the microlens. The maximum deviation of the beam in x and y directions are given as ±38.5 pixels. From the illuminating beam size and the focal lengths of the tested samples, it is expected that the converging angles of the reflected beam from the samples are 6.48˚, 2.86˚ and 4.6˚ for the spherical mirror, analog HOE and DHOEs, respectively. The angle 6.48˚ for the spherical mirror is much bigger than the maximum beam incidence angle 4.29˚ of the microlens. This means that the beam at its edge side may make light spots at the neighboring 77 x 77 pixels arrays to its corresponding array. For the DHOEs, the converging angle is slightly bigger than the 4.29˚. So, the very edge part of the beam may focus at the neighboring arrays. The light spot position in each pixel array, obtained by the centroid calculation provides the wavefront deviation from its ideal wavefront. The deviation can be used to either draw the phase map for visual estimation of the wavefront aberration or Zernike polynomial to see the aberration components. However, since the deviation can comprise not even that from the material to be tested but also from the illumination beam of the material, the latter should be removed from the total aberration to find the aberration only from the material. The typical illumination beam to the material is a collimated laser beam because it is considered that the beam does not introduce any wavefront aberration when it is ideally collimated. But it is difficult to make an ideal collimated beam, the wavefront of the collimated beam needs to be measured in advance with the sensor, its aberration contribution should be removed from the total aberration. The notable aberration components are spherical aberration, coma, defocus, tilt and astigmatism, The polynomial allows viewing each of these aberrations individually

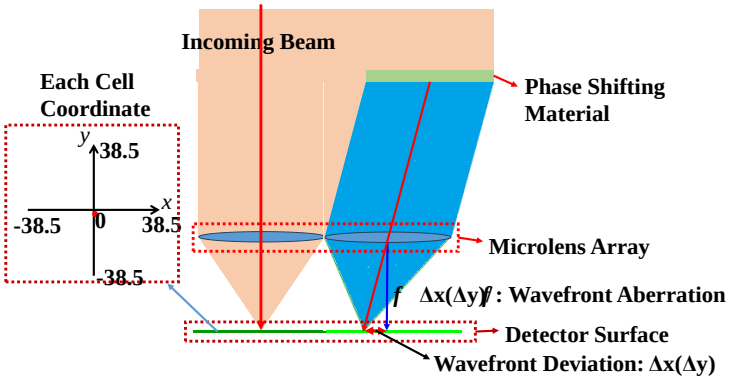

Figure 3. Wavefront aberration and principle of Shack-Hartmann wavefront sensor.

3. ZERNIKE POLYNOMIAL

In general, when a beam $E_0(x,y)\exp(-i\omega t + i\frac{2\pi}{\lambda}\varphi(x,y)$ is normally incident to a material, the reflected /transmitted beam from the material can be expressed as,

$$E(x,y) = \alpha E_0(x,y)\exp(-i\omega t \pm i\frac{2\pi}{\lambda}\big(\varphi(x,y) + w(x,y)\big), \quad (1)$$

Where $\varphi(x,y)$, α, λ and $w(x,y)$ are the initial phase of the beam, the reflectivity/transmissivity of the material, the wavelength of the beam and the wavefront aberration introduce by the material. respectively. $w(x,y)$ is expressed as [11].

$$w(x,y) = \sum_{j=1}^{n} W_j \, \Phi_j(\rho,\theta), \tag{2}$$

where $\Phi_j(\rho,\theta)$ are j[th] component of Zernike polynomial in polar coordinate and W_j the coefficient of j[th] component. $w(x,y)$ is defined within a unit circle. The Zernike polynomial $\Phi(\rho,\theta)$ is given as [10],

$$\Phi(\rho,\theta) = A_0^0 + \sum_{q=1}^{\infty} A_{2q}^0 R_{2q}^0(\rho) + \sum_{n=1}^{\infty} \sum_{l=1(2)}^{n} [A_n^l R_n^l(\rho) cosl\theta + B_n^l R_n^l(\rho) sinl\theta], \tag{3}$$

where, $A_n^l(l \geq 0) = \sqrt{\frac{2(n+1)}{1+\delta_{l0}}}1$, $B_n^l = -A_n^l(l<0)$, $R_n^l(\rho) = \sum_{s=0}^{(n-|1|)/2} \frac{(-1)^s (n-s)!}{s!\left\{\frac{n+|1|}{2}-s\right\}!\left\{\frac{n-|1|}{2}-s\right\}!} \rho^{n-2s}$, and $l = 1,3,5,7, \bullet, \bullet, \bullet, n|_{\text{for odd } n}$ and $l = 2,4,6,8, \bullet, \bullet, \bullet, n|_{\text{for even } n.}$ $R_n^l(\rho)$ is Zernike polynomial in polar coordinate A_n^l and B_n^l, coefficient of decomposition that determine wave aberration value of the n[th] of order. If l=0 (the second term in right part of eq. (3)), n must be even (n=2q). If the deviation of the focused beam spot in a 77 x 77 pixel array is given as (x_m, y_m), the slope (x_m/f, y_m/f) is expressed as,

$$\frac{x_m}{f} = \frac{\partial \Phi(\rho,\theta)}{\partial x}, \qquad \frac{y_m}{f} = \frac{\partial \Phi(\rho,\theta)}{\partial y} \tag{4}$$

Eq.4 can be written as,

$$\frac{\partial \Phi(\rho,\theta)}{\partial x} = \frac{\partial \Phi(\rho,\theta)}{\partial \rho}\frac{\partial \rho}{\partial x} + \frac{\partial \Phi(\rho,\theta)}{\partial \theta}\frac{\partial \theta}{\partial x}, \quad \frac{\partial \Phi(\rho,\theta)}{\partial y} = \frac{\partial \Phi(\rho,\theta)}{\partial \rho}\frac{\partial \rho}{\partial y} + \frac{\partial \Phi(\rho,\theta)}{\partial \theta}\frac{\partial \theta}{\partial y} \tag{5}$$

In polar coordinate, $\rho = \sqrt{x^2+y^2}$, $x = \rho cos\theta \;\; and \;\; y = \rho sin\theta$. Hence,

$$\frac{\partial \Phi_{2q}^0(\rho,\theta)}{\partial x} = \cos\theta \frac{\partial R_{2q}^0(\rho)}{\partial \rho} \tag{6}$$

$$\frac{\partial \Phi_n^l(\rho,\theta)}{\partial x} = A_n^l\{\cos\theta\cos l\theta \frac{\partial R_n^l(\rho)}{\partial \rho} + l\sin\theta\sin l\theta \frac{R_n^l(\rho)}{\rho}\} + B_n^l\{\cos\theta\sin l\theta \frac{\partial R_n^l(\rho)}{\partial \rho} - l\sin\theta\cos l\theta \frac{R_n^l(\rho)}{\rho}\} \tag{7}$$

$$\frac{\partial \Phi_{2q}^{0}(\rho,\theta)}{\partial y} = \sin\theta \frac{\partial R_{2q}^{0}(\rho)}{\partial \rho} \tag{8}$$

$$\frac{\partial \Phi_{n}^{l}(\rho,\theta)}{\partial y} = A_n^l\{\sin\theta\cos l\theta \frac{\partial R_n^l(\rho)}{\partial \rho} - l\cos\theta\sin l\theta \frac{R_n^l(\rho)}{\rho}\} + B_n^l\left\{\sin\theta\sin l\theta \frac{\partial R_n^l(\rho)}{\partial \rho} + l\cos\theta\cos l\theta \frac{R_n^l(\rho)}{\rho}\right\} \tag{9}$$

$$\frac{\partial \Phi(\rho,\theta)}{\partial x} = \sum_{q=1}^{\infty}\cos\theta \frac{\partial R_{2q}^{0}(\rho)}{\partial \rho} + \sum_{n=1}^{\infty}\sum_{l=1(2)}^{n}[A_n^l\{\cos\theta\cos l\theta \frac{\partial R_n^l(\rho)}{\partial \rho} + l\sin\theta\sin l\theta \frac{R_n^l(\rho)}{\rho}\} + B_n^l\{\cos\theta\sin l\theta \frac{\partial R_n^l(\rho)}{\partial \rho} - l\sin\theta\cos l\theta \frac{R_n^l(\rho)}{\rho}\}] \tag{10}$$

$$\frac{\partial \Phi(\rho,\theta)}{\partial y} = \sum_{q=1}^{\infty}\sin\theta \frac{\partial R_{2q}^{0}(\rho)}{\partial \rho} + \sum_{n=1}^{\infty}\sum_{l=1(2)}^{n}[A_n^l\{\sin\theta\cos l\theta \frac{\partial R_n^l(\rho)}{\partial \rho} - l\cos\theta\sin l\theta \frac{R_n^l(\rho)}{\rho}\} + B_n^l\{\sin\theta\sin l\theta \frac{\partial R_n^l(\rho)}{\partial \rho} + l\cos\theta\cos l\theta \frac{R_n^l(\rho)}{\rho}\}] \tag{11}$$

From Eqs. 3 to 11, the Zernike polynomial for different *n* and *l* values are calsulated and they are listed in Table 1.

Table 1. Some components of Zernike polynomial. Both polar and Cartesian coordinate expressions are given.

n	l	$\phi(\rho,\theta)$	Remark
0	0	1 [1]	Constant Term or Piston
1	-1	$2\rho\sin\theta$ [$2y$]	Tilt in y-direction, Distortion
1	1	$2\rho\cos\theta$[$2x$]	Tilt in x-direction, Distortion
2	-2	$\sqrt{6}\rho^2\sin 2\theta$[$\sqrt{6}(2xy)$]	Astigmatism 45^0
2	0	$\sqrt{3}(2\rho^2-1)$ [$\sqrt{3}(2(x^2+y^2)$-1)]	Field Curvature, Defocus
2	2	$\sqrt{6}\rho^2\cos 2\theta$[$\sqrt{6}(x^2-y^2)$]	Astigmatism in 0^0 or 90^0 axis
3	-3	$\sqrt{8}\rho^3\sin 3\theta$[$\sqrt{8}(3yx^2-y^3)$]	Trefoil y
3	-1	$\sqrt{8}(3\rho^3-2\rho)\sin\theta$[$\sqrt{8}(3(x^2+y^2)-2)y$]	Coma along y-axis
3	1	$\sqrt{8}(3\rho^3-2\rho)\cos\theta$[$\sqrt{8}(3(x^2+y^2)-2)x$]	Coma along *x*-axis
3	3	$\sqrt{8}\rho^3\cos 3\theta$[$\sqrt{8}(x^3-3y^2x)$]	Trefoil *x*
4	-4	$\sqrt{10}\rho^4\sin 4\theta$[$\sqrt{10}(4x^3y-4xy^3)$]	Tetrafoil y
4	-2	$\sqrt{10}(4\rho^4-3\rho^2)\sin 2\theta$[$\sqrt{10}(8xy(x^2+y^2)-6xy)$]	Secondary Astigmatism
4	0	$\sqrt{5}(6\rho^4-6\rho^2+1)$[$\sqrt{5}(6(x^2+y^2)^2-6(x^2+y^2)+1)$]	Spherical Aberration, Defocus
4	2	$\sqrt{10}(4\rho^4-3\rho^2)\cos 2\theta$[$\sqrt{10}(4(y^4-x^4)-3(y^2-x^2)$]	Secondary Astigmatism
4	4	$\sqrt{10}\rho^4\cos 4\theta$[$\sqrt{10}(x^4-6x^2y^2+y^4)$]	Tetrafoil $x(0^0)$
		$\rho^4\cos 4\theta$[$x^4+y^4-6x^2y^2$]	
		$\rho^4\sin 4\theta$[$4(x^2-y^2)$ xy]	

Based on these components of Zernike polynomial, the wavefront aberration in Eq. 2 can be calculated by finding the coefficient $W_j|_{j=1 \text{ to } n}$. Since the component values of the polynomial are found by substituting deviation values, finding the coefficient W_j for the n components of the polynomial requires n set of deviation values. This means that the minimum number of microlenses in a horizontal direction of the microlen array should be n. It also be needed n microlenses in the vertical direction. So. the number of calculations needed to find W_j becomes proportional to n^2. Huge matrix calculation should be performed as n increases.

4. PHASE MAPS AND WAVEFRONT ABERRATION

Fig. 4(a) shows the light spot array and 4(b) the centroid calculated from the array. The spot array consistes of 51 x 77 light spots. However, there are many defected light spots in edge parts of the array due to the spoiled microlenses. To eliminate spoiled spots, only 43 x 69 light spots array is processed for further use. Furthermore, the light spot in each 77 x 77 pixels-array do not have a circular dot shape but somewhat distributed. So, the probable focal spot from the distribution will be found by centroid calculation. For the centroid calculation, the boundaries of the 77 x 77 pixels-array for each light spot should be defined in advance. Fig. 4(b) shows the boundaries, the center of each light spot and the centroid position. It shows only 5 x 5 light spots out of 51 x 77 array in Fig. 4(a) to clearly show the centroid deviation. The red square represents the center of each array, the blue square is the centroid found by different methods, and the green square by typical centroid finding method. Each square size is 7 x 7 pixels. The blue and green squares match well between them and show clear deviation from the red square.

From the centroid positions shown in Fig. 4, the centroid distributions for the four samples in Fig. 2 including the collimating beam are calculated and then the phase maps are drawn. The phase map is a grouped presentation of the centroid position from the position of its pixel array. Two groupings are introduced here; one is grouping 2.5 pixels deviation interval and λ pathlength difference interval between rays from each microlens. The ray normally incident to the microlens center will be reached to the mid- position of the 77 x 77 pixels-array. However, the ray with an incident angle will travel longer distance than the normal ray to reach the array, because it is away from the mid position. So, the centroid position deviations corresponding to the pathlength differences of λ, 2λ, 3λ, and so on. The λ, 2λ, and 3λ differences corresponding to 11.86, 16.77 and 20.54- pixels deviations. When the pathlength difference is more than 7λ, the λ increase provides less than 2.5 pixels deviation interval will be good for the overall centroid position deviation is small but for the λ pathlength interval, large. Figs. 5 to 7 show the collimated deviation distributions, phase maps and reconstructed wavefronts of the four samples including the collimated beam. Fig. 5 is for the collimated beam, Fig. 6 for spherical mirror and analog HOE, Fig. 7 for DHOE 1 and 2. Fig. 5 shows two collimated beams. Beam1 is the collimated beam for the spherical mirror, analog HOE and DHOE 1, and beam 2 for DHOE 2. The centroid position deviation is slightly smaller for Beam 2 The smaller means it is better collimated. The ideally collimated beam will make no rings but white color only because there will not be any deviation. The deviation distribution directions are almost the same for both beam 1 and 3. . They are making around 27° with the horizontal direction. In phase maps, the different color rings are somewhat noisy but they are making near circular shape. The colors white, blue, green, red, sky blue, pink and yellow represent the pixel deviations of 0 to 2.5, <2.5 to 5.0, <5.0 to 7.5, < 7.5 to 10, <10 to 12.5, <12,5 to 15 and <15 to 17.5, respectively. The reconstructed wavefronts are also similar either beam 1 or 2 is rotated 180°.

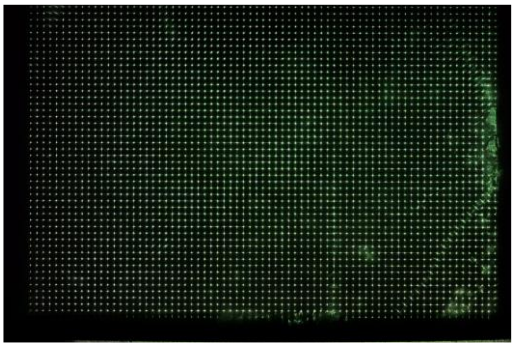

(a) Light Spot Array
(Output of S-H sensor)

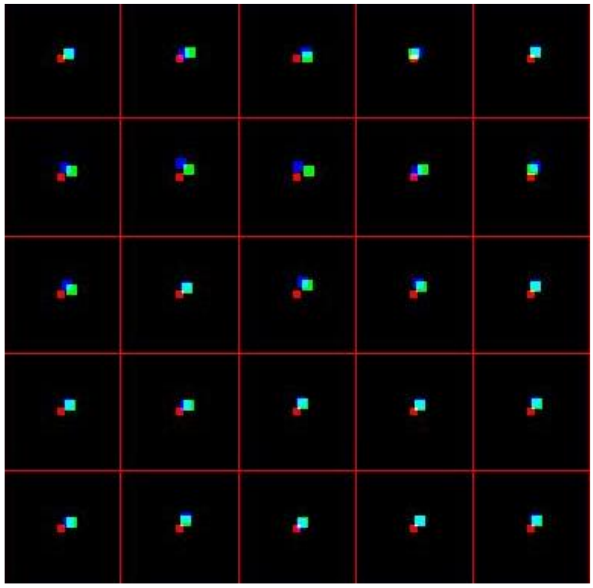

(b) Centroid array

Figure 4. Light spot and centroid arrays.

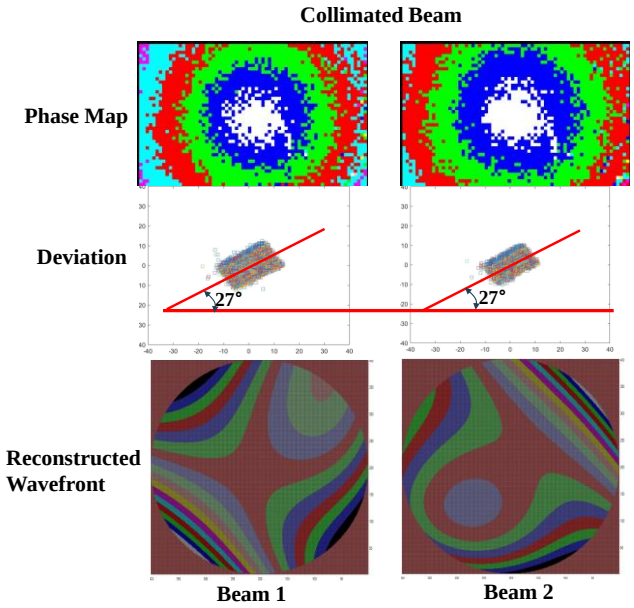

Figure 5. Collimated beam' phase maps, deviations and reconstructed wavefronts

Fig. 6 shows three phase maps each: Left one is drawn with 2.5 pixels interval. The mid one is the λ pathlength difference and right λ pathlength difference but compensated, i.e., the collimated beam's deviation is subtracted from the that of the spherical mirror/analog HOE. Since the 38.5 pixels distance corresponds to 16 rings for the 2.5 pixels interval and 11 rings for the λ pathlength difference, for the spherical mirror, the number of rings should be 11 in horizontal direction but for the analog HOE, 5 rings because it's converging angle is 2.86°. In Fig. 6, the rings for spherical mirror is 11 for the 2.5 pixels interval but 5 for the λ pathlength. This number are much smaller than the theoretical prediction. However, when the deviation is compensated, very clear, i.e., no noises, especially in the left side of the rings and near circular shape concentric rings are appearing and it's numbers are reached to 9. This number is still smaller than the theoretically predicted number but the reason is not found yet. The deviation distribution makes around 10° down siding but it is aligned to horizontal direction and the deviation is increases from 20th pixel range to 30th pixel range. For the analog HOE, only 6 rings for 2.5 pixels interval, but only 3 rings for the λ pathlength. However, when it is compensated the ring number becomes 5, which corresponds to the expected and the ring shapes becomes near circular, though there are some noises in each ring. The deviation distribution also makes around 15° down siding but it is also aligned to horizontal direction and the deviation is increases from 10th pixel range to 20the pixel range. The deviation distributions in Fig. 6 indicates that the collimated beam's degree of collimation affects tremendously to the wavefront of the samples. It should be compensated. The reconstructed wavefronts informs that the symmetricity of wavefronts is much improved. This means that the collimated beam's wavefront introduced distortion to the samples' wavefronts. It is considered that the reconstructed wavefront of the spherical mirror has a better symmetricity than that of the analog HOE. Two facing patterns along 135° diagonal which have positive values and 45° diagonal which has the negative values is very symmetric for the spherical mrror than the analog HOE.

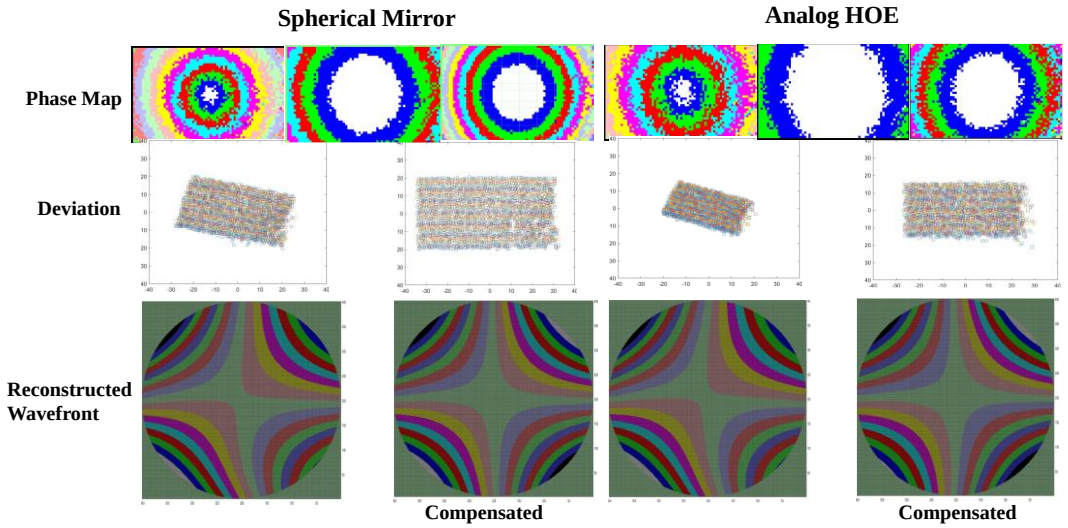

Figure 6. Phase maps, deviations and reconstructed wavefronts of the spherical mirror and analog HOE

Fig. 7 also shows three phase maps for each of DHOE 1 and 2: Three phase maps for each sample are arranged the same order as those in Fig. 6. Since the converging angle of the DHOE 1 and 2 is 4.6° which is bigger than the maximum beam incidence angle to each microlens, 4.29°, the expected number of rings for 2.5 pixels interval is 16 and the λ pathlength difference 11.

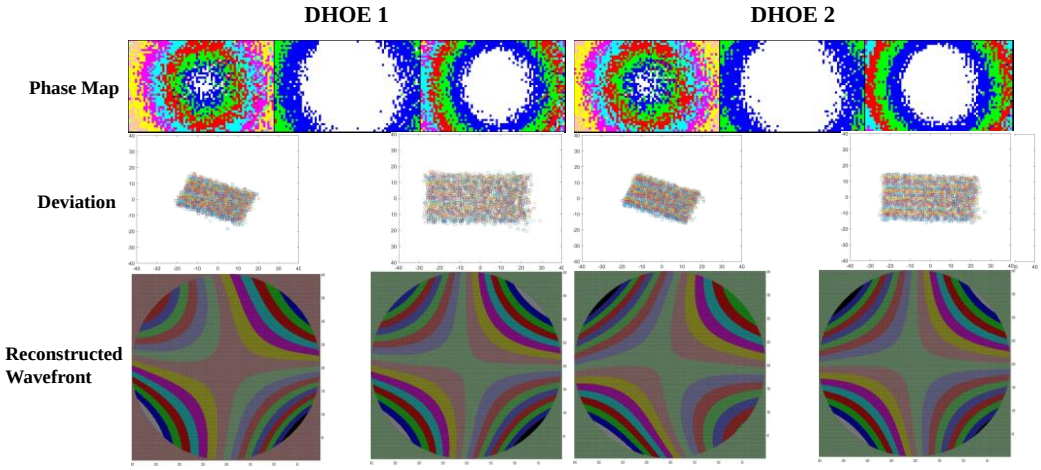

Figure. 7. Phase maps, deviations and reconstructed wavefronts of the DHOE 1 and 2.

As shown in Fig. 7, the number of rings for the 2.5 pixels is 7 and very noisy, and barely 3 for the λ pathlength difference. When it is compensated, the number of rings are barely 5 but noisy. The DHOE 2 looks less noisy than the DHOE 1 but its ring number is 4. The presence of noises are probably caused by the nonuniform distribution and shapes of the hogels. The smaller number of rings compared with their theoretically predicted number indicates that the converging power of DHOE 1 and 2 is much smaller than that of the Analog HOE. The deviation distribution makes around 17° down side for both DHOE 1 and 2. This down sided angle is bigger than those of the spherical mirror and analog HOE. This is why the compensated deviation distributions are also slightly down sided. The reconstructed

wavefront reveals that the symmetricities of the patterns are worse than those of the spherical mirror and the analog HOE because 135° direction patterns and 45° direction patterns do not have the same absolute value. In fact, the negative value side patterns have higher peak than the positive. The difference is worse for DHOE 1 than the 2. The symmetricity of two facing pattern is very worse compared with the spherical mirror and the analog HOE.

The 16 coefficient values of these samples shows that they are mostly in the range of 10^{-2} and 10^{-3} [3]. The values are smaller for the spherical mirror and, in general. analog HOE.

5. CONCLUSIONS

The reconstructed wavefront by Zernike polynomial does not show the wavefront differences among the samples, at a glance. However, the symmetricity of the composing patterns clearly shows that it is deteriorating in the order of the spherical mirror, analog HOE, and DHOE 2 and 1. In contrast to the polynomial, the phase map can tell at a glance the differences among the samples, though it cannot describe different wavefront aberrations as the polynomial. The phase map can tell how well the samples can be converged, and how much distortions and noises will be introduced by the samples. The digital HOEs can perform their function as spherical mirrors/lens, but their optical qualities will be worse than the spherical mirror and the analog HOE at least in current stage.

ACKNOWLEDGEMENTS

Priority Reseach Centers Program through the National Reseach Foundation of Korea (NRF) funded by the Ministry of Education (Grant Number: NRF-2018R1A6A1A03025542).

REFERENCES

[1] Son, J.-Y., Son, W.-H., Kim, S.-K., Lee, K.-H. and Javidi, B. “3-D imaging for creating real world like environments,” Proceedings of The IEEE (Invited) 101(1), 190-205 (2013).
[2] Komar, V. G., and Serov, O. B., [Art Holography and Holographic Cinematograthy], Iskusstvo, Moscow, (1990).
[3] Lee, B.-R., Marichal-Hernández, J. G., Rodríguez-Ramos, J. M., Son, W.-H., Hong, S., Son, J.-Y., “Wavefront Characteristics of a Digital Holographic Optical Element,” Micormachines 14, 1229 (2023).
[4] Dallas, W. J., [Computer Generated Holograms], Springer-Verlag, Berlin, Germany, (1980).
[5] Rousset, G., “Wavefront sensing,” in Alloin D. M., and Mariotti, J.-M., [Adaptive Optics for Astronomy], NATO ASI Series, Kluwer Academic, 116-137 (1994).
[6] Son, J.-Y., Podanchuk, D.V., Dan’ko, V.P., and Kwak, K.-D., “Shack-Hartmann wave-front sensor with holographic memory,” Optical Engineering 42(11), 3389-3398 (2003).
[7] Wood, R. B., and Hayford, M. J., "Holographic and Classical Head Up Display Technology for Commercial and Fighter Aircraft," Proc. SPIE 883, 36-5 (1988).
[8] Smirnov, V.V., Son, J.-Y., Jeon, H.-W., Lee, H.-S., and Choi, Y.-J., "A Full Color Reflection Type Holographic Screen," Proc. SPIE 3293, 175-182 (1998).
[9] Klug, M. A., Newawanger, C., Huang, Q., Holzbach, M.E., “Active digital hologram displays,” Zebra Imaging Inc, U.S. Patent US7227674B2, 1-15 (2007).
[10] Podanchuk, D. V., Dan’ko, V. P., Kotov, M. M., Son J.-Y., and Choi, Y.-J., “Extended-range Shack-Hartmann wavefront sensor with nonlinear holographic lenslet array,” Optical Engineering 45(6), 053605-1-053605-5, (2006).
[11] Lee, B.-R., Marichal-Hernández, J. G., Rodríguez-Ramos, J. M., Venkel, T., and Son, J.-Y., "Compensation of wavefront aberration introduced by DMDs’ operation principle," Optical Materials 140, 113863 (2023).